RSC Advances

PAPER

View Article Online
View Journal | View Issue

Cite this: *RSC Adv.*, 2023, **13**, 16758

Theoretical prediction on net boroxene as a promising Li/Na-ion batteries anode

Chunlai Huang,[ab] Junping Hu *[ab] and Chuying Ouyang[c]

Novel two-dimensional (2D) electrode materials have become a new frontier for mining electrode materials for Li-ion batteries (LIBs) and Na-ion batteries (NIBs). Herein, based on first-principles calculations, we present a systematic study on the Li and Na storage behaviors in Calypso-predicted completely flat 2D boron oxide (l-B_2O) with large mesh pores. We start our calculations from geometrical optimization, followed by a performance evaluation of Li/Na adsorption and migration processes. Finally, the specific capacity and average open-circuit voltage are evaluated. Our study reveals that l-B_2O has good electrical conductivity before and after Li/Na adsorption and the Li/Na diffusion barrier height and average open-circuit voltage are both low, which is beneficial to the rate performance and full-cell operation voltage, respectively. Furthermore, it suffers a small lattice change (<1.7%), ensuring good cycling performance. In particular, we find that the Li and Na theoretical specific capacities of l-B_2O can reach up to 1068.5 mA h g^{-1} and 712.3 mA h g^{-1}, respectively, which are almost 2–3 times higher than graphite (372 mA h g^{-1}). All the above outcomes indicate that 2D l-B_2O is a promising anode material for LIBs and NIBs.

Received 6th May 2023
Accepted 22nd May 2023

DOI: 10.1039/d3ra03007e

rsc.li/rsc-advances

1. Introduction

New energy storage technologies can effectively avoid the intermittency of renewable energy power generation and help smooth out user demand to boost energy utilization efficiency,[1–5] among which lithium-ion batteries are key components for mobile electrical devices, EVs, and large-scale energy storage stations.[6–10] However, as the demand for energy storage continues to grow, the existing Li resources fall short in meeting the demand, leading to a significant increase in the cost of LIBs.[11] Considering this, Na ion batteries are expected to achieve partial substitution among small and micro EVs and large energy storage stations in view of their comparatively lower prices and abundant Na resources.[12,13]

Whether it concerns LIBs or NIBs, the most critical material is still the electrode material. Good electrode materials are conducive to achieving high specific capacity and high power, thus realizing fast and large charging mode.[14] Electrode materials are divided into positive and negative electrode materials. At present, the research on positive electrode materials is relatively abundant, but the research on negative electrode materials is relatively small.[15,16]

With the discovery of graphene,[17] more and more 2D materials have been successfully prepared. The emergence of these 2D materials has given more possibilities to optimize the electrode materials for secondary batteries due to their large specific surface area and high electronic conductivity, making it possible to store large amounts of metal ions for higher capacity.[18] The diffusion rate of metal ions along the surface of 2D materials is generally fast, which facilitates the rate performance.[19] More importantly, 2D electrode nanomaterials do not show large volume changes during battery charging and discharging, thus maintaining structural integrity during cycling.[20] Therefore, in recent years, 2D materials have been intensively studied in the field of energy storage devices.[21,22]

For negative electrode materials, to obtain higher theoretical capacity, their own atomic weight should be relatively low, for example, among all 2D materials, boron-based 2D materials are predicted to have the highest theoretical capacity at present.[23] Recently, we used Calypso,[24] a very popular material structure prediction software, to obtain a new type of 2D material that is more stable in energy than its counterpart two-dimensional boron oxide of the same scale.[25] It is worth noting that due to the electron-deficient nature of boron atoms, which makes B–B bonds unstable in borophene,[26,27] and the experimental results that B–O bonds are more stable than B–B bonds under oxygen-rich conditions,[28] the possibility of the experimentally successful preparation of 2D "B_xO_y" predicted by Calypso is increasing; therefore, there are more and more theoretical and experimental studies on 2D "B_xO_y" materials,[29,30] including 2D B_2O. To the best of our knowledge, our predicted 2D B_2O here has not

[a]*Nanchang Key Laboratory of Photoelectric Conversion and Energy Storage Materials, Nanchang Institute of Technology, Nanchang 330099, China*
[b]*Key Laboratory of Optoelectronic Materials and New Energy Technology, Nanchang Institute of Technology, Nanchang 330099, China*
[c]*Department of Physics, Laboratory of Computational Materials Physics, Jiangxi Normal University, Nanchang 330022, China*

been studied regarding the direction of electrode materials for LIBs or NIBs.

Motivated by the discussions above, herein, using first-principles calculations, we systemically examine the Li and Na storage behaviors in completely flat 2D boron oxide (l-B_2O) with large mesh pores. We start our calculations from geometrical optimization, followed by the performance evaluation of Li/Na adsorption and migration processes. Finally, specific capacity and average open-circuit voltage are evaluated. Our study reveals that l-B_2O has good electrical conductivity before and after Li/Na adsorption, the Li/Na diffusion barrier height and average open-circuit voltage are both low, which is beneficial to the rate performance and full-cell operation voltage, respectively. Furthermore, it suffers a small lattice change (<1.7%), ensuring good cycling performance. In particular, we find that the Li and Na theoretical specific capacities of l-B_2O can reach up to 1068.5 mA h g^{-1} and 712.3 mA h g^{-1}, respectively, which are almost 2–3 times higher than graphite (372 mA h g^{-1}). All the above outcomes indicate that 2D l-B_2O is a promising anode material for LIBs and NIBs.

2. Computational methods

The structural predication of the l-B_2O was obtained *via* crystal structure analysis performed by particle swarm optimization (CALYPSO).[31–33] Just based on the given chemical composition, the CALYPSO code can efficiently search out the ground or metastable structures. All key parameters are chosen from the default values of Calypso software. For example, PopSize = 30 and Kgrid = 0.12 0.06. Our first-principles calculations are based on the density functional theory with the plane-wave pseudopotentials[34,35] realized in the Vienna *Ab initio* Simulation Package (VASP).[36,37] The exchange-correlation functional is modeled in the generalized gradient approximation (GGA) with the Perdew-Burke-Ernzerhof (PBE)[38,39] realization. Boron $2s^2 2p^1$, oxygen $2s^2 2p^6$, lithium $2s^1$, and sodium $3s^1$ electrons are treated as valence electrons. A 520 eV cutoff energy is used for the plane wave expansion of the wave functions. The Brillouin zone is sampled with $3 \times 3 \times 1$ and $5 \times 5 \times 1$ mesh Monkhorst–Pack *k*-point mesh[40] for the structural optimization and electronic structure calculations, respectively. The criteria of convergence for the energy and forces are 10^{-5} eV and 10^{-3} eV $Å^{-1}$, respectively. Phonon spectra calculations were conducted with the Phonopy package.[41]

3. Results and discussion

3.1 Lattice structure

After total relaxation, the lattice structure for l-B_2O is shown in Fig. 1(a) and (b). For the optimized 2×2 supercell, which contains 16 B atoms and 8 O atoms, the corresponding lattice constants are $a = b = 10.822$ Å, the rhombic cell angle is 138.638°, as shown in Fig. 1(a), and the individual bond lengths are 1.571 Å (b_1), 1.569 Å (b_2), 1.623 Å (b_3), 1.477 Å (b_4), and 1.704 Å (b_5). As shown in Fig. 1(a), the atomic structure of l-B_2O possesses completely planar net configuration, and its space group is *Amm*2 (no. 38). The electron localization function (ELF) is illustrated in Fig. 1(c), showing that each O atom is strongly bonded to three adjacent B atoms and between B and B atoms. The phonon spectrum of l-B_2O shows no imaginary frequency modes, as plotted in Fig. 1(d); hence, this configuration is dynamically stable. Moreover, by comparing the total energy of the system with other B_2O-type structures[42,43] of the same chemical composition, we found that l-B_2O is 0.12 eV per unit lower in total energy than their proposed structure. This implies that l-B_2O is more stable energetically. This means that l-B_2O is

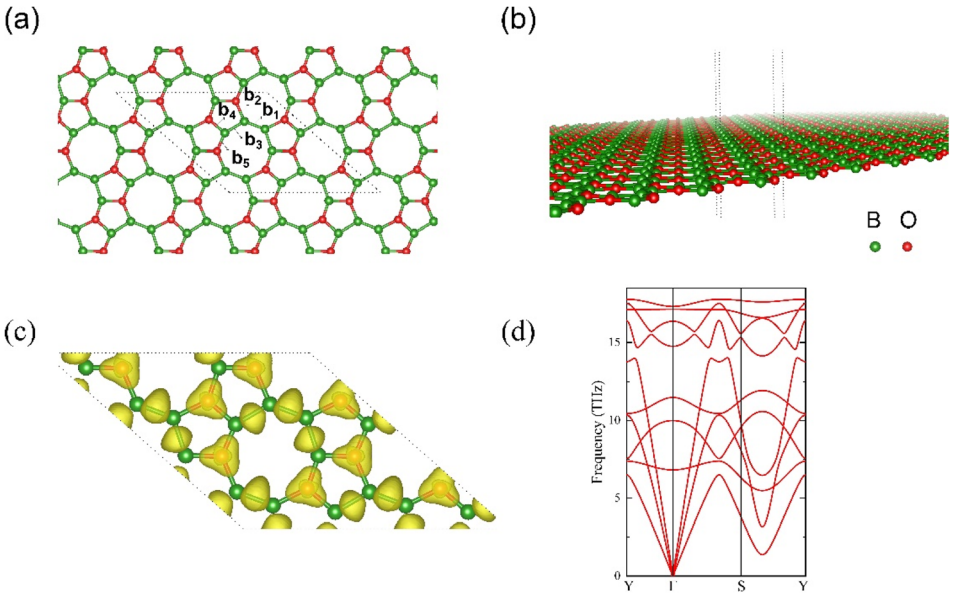

Fig. 1 (a and b) Are given for the side and top views of optimized structure of flat boron oxide (l-B_2O), and (c) its electron localization function (ELF) and (d) phonon spectrum curve. In (a and b), the green balls are B elements, and red balls are O atoms. The grey dashed line outlines the 2×2 supercell for l-B_2O.

more energetically stable, and since the experimental synthesis is still in the exploratory stage, this is more conducive to the successful experimental preparation of l-B_2O by chemical vapor deposition (CVD), hydrothermal synthesis, solvothermal method, mechanical stripping, and redox stripping.[44]

3.2 Li or Na adsorption

To initially clarify whether l-B_2O can be used as an electrode material for Li/Na ion batteries or whether it is more suitable as a cathode or anode material, it is necessary to investigate the adsorption behavior of individual Li or Na atoms on the l-B_2O monolayer. Depending on the atomic structure symmetry, three possible types of adsorption sites are regarded, *i.e.*, hollow sites (above the center of B/O five-membered ring or eight-membered ring), top sites (above B or O atoms), and bridge sites (above the B–O bond center).

The adsorption properties are given by the estimation of the adsorption energies, the definition is as follows.

$$E_{ad} = E_{B_{16}O_8} - E_{B_{16}O_8M} - E_M \quad (1)$$

where M denotes Li or Na, E_M is the average energy of Li atoms in Li or Na metals, and $E_{B_{16}O_8}$ is the total energies of l-B_2O. $E_{B_{16}O_8M}$ is the total energies of l-B_2O after M adsorption. All the total energies are based on completely structural optimizations.

A negative E_{ad} value implies that Li or Na can spontaneously adsorb on the l-B_2O without forming a cluster; in contrast, its positive values suggest that Li or Na is more inclined to form clusters. By comparing the magnitude of the adsorption energy, we determined the most stable configuration for Li or Na adsorption, as shown in Fig. 2(c) and (d), in which the Li or Na atom are both located above the hollow site of the B–O–B ring. The Li adsorption energy are −0.17 eV, and the Na adsorption energy is −0.20 eV, implying that l-B_2O has a great possibility to be utilized as the LIBs/NIBs anode. In addition, we performed Bader charge analysis calculations, which is tabulated in Table 1 and reveals that about 0.86*e* and 0.88*e* are shifted to the $B_{16}O_8$ monolayer after the adsorption of Li and Na, respectively. To better understand the interaction behavior between Li/Na and 2D l-B_2O, as shown in Fig. 2(e) and (f), we drew the charge density difference curves for the two most stable adsorption conformations. It can be seen that the electrons in both adsorption configurations tend to cluster around the B–O–B ring, while their density decreases around the Li or Na atoms. Both results indicate a strong interaction between Li (Na) and $B_{16}O_8$ monolayers, which is favorable for the high capacity obtained.

Table 1 Bader charge analysis

	Average charge state			
	B	O	Li	Na
$B_{16}O_8$	2.211	7.577		
$LiB_{16}O_8$	2.259	7.590	0.136	
$Li_8B_{16}O_8$	2.584	7.628	0.204	
$NaB_{18}O_9$	2.258	7.593		0.119
$Na_8B_{16}O_8$	2.459	7.626		0.454

Moreover, we execute the electronic structure calculations for $B_{16}O_8$ and its most stable Li/Na adsorption configurations of l-B_2O, *i.e.*, $B_{16}O_8Li/B_{16}O_8Na$, because it is important for its function as electrodes for LIBs or NIBs. The results are shown in Fig. 3. As we can see, for $B_{16}O_8$, there is an energy gap of 0.13 eV near the Fermi energy level, which still indicates that $B_{16}O_8$ has good electronic conductivity. Crucially, this energy gap disappears when Li or Na is adsorbed, which means that the electronic conductivity becomes better and that most of the

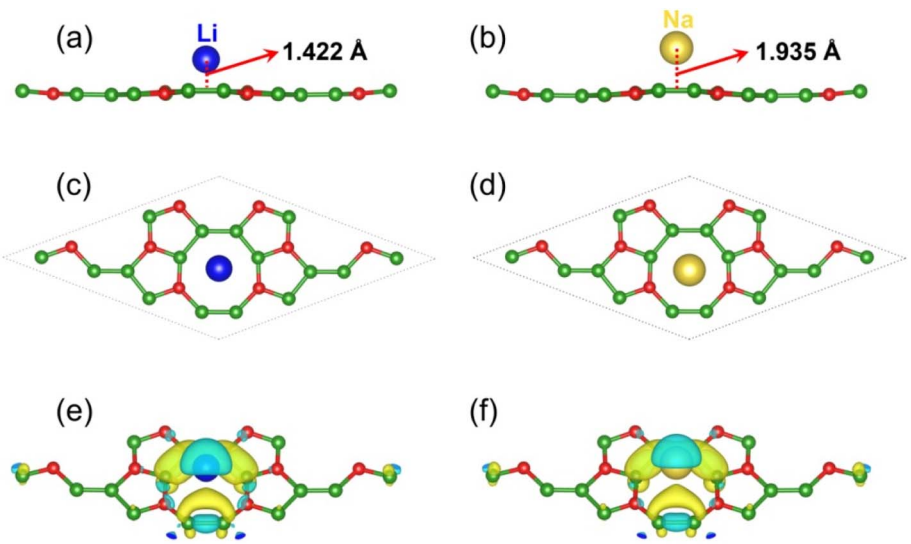

Fig. 2 (a) Side view of the most stable Li adsorption configuration; (b) side view of the most stable Na adsorption configuration; (c and d) are the corresponding top views of the configurations in (a and b); (e and f) corresponding charge density difference profiles, calculated by $\rho = \rho_{B_{16}O_8M} - \rho_{B_{16}O_8} - \rho_M$, M = Li, Na. $\rho_{B_{16}O_8M}$, $\rho_{B_{16}O_8}$, and ρ_M are the total charge of the system, $B_{16}O_8$ and Li atom, respectively. The blue and yellow areas represent electron losses and gains.

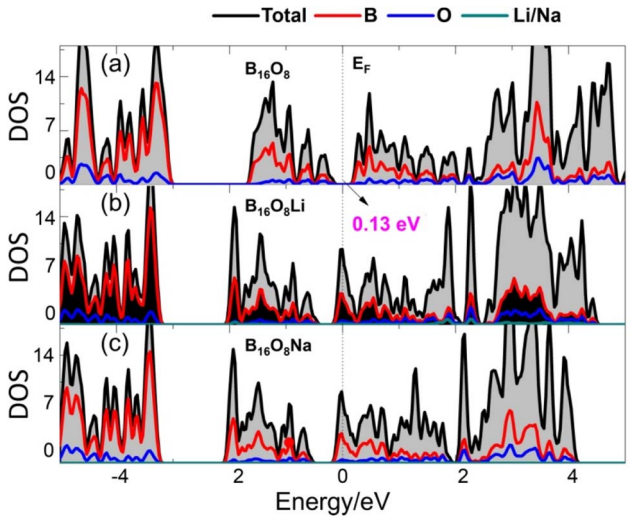

Fig. 3 Density of states (DOS) for (a) $B_{16}O_8$ and its lithiated and sodiated phase, *i.e.*, (b) $B_{16}O_8Li$ and (c) $B_{16}O_8Na$.

electronic states near the Fermi energy level are contributed by the B atom.

3.3 Li or Na diffusion

It is well-known that rate performance is another key parameter of Li- or Na-ion batteries. To evaluate it, we performed the calculation of the diffusion barrier, *i.e.*, we determined the optimal path of diffusion and calculated its corresponding diffusion barrier using the climbing image nudged elastic band (CL-NEB) method.[45] For l-B_2O monolayer utilized as the Li-ion batteries electrode material, we consider the three pathways representing all the possible diffusion paths, as shown in Fig. 4(a). The initial and final states are both the most stable Li/Na adsorption configurations. The corresponding energy barriers for Li migration are plotted in Fig. 4(b), where the saddle points for each path are found. Similarly, for l-B_2O monolayer utilized in Na-ion batteries, the energy barriers and migration pathways profiles are shown in Fig. 4(c), and the saddle points are also found for each path. Obviously, the Li diffusion barriers are higher than that of the Na diffusion barrier for each corresponding migration way. For both cases, the path 3 migration ways possess the lowest diffusion barrier, which is 0.38 eV for Li and 0.25 eV for Na.

The above calculation results suggest fast Li or Na diffusion on l-B_2O, which is expected to give good rate performance of l-B_2O as an anode. To better explain the energy barriers, we relate the calculated Li or Na migration energy barriers with diffusion coefficients, expressed as follows.[46–48]

$$D = d^2 \nu_0 e^{\left(-\frac{E_a}{k_B T}\right)} \quad (2)$$

where d is the migration distance of the above pathways, E_a is the diffusion barrier, k_B is the Boltzmann constant, T is absolute temperature, and ν_0 is the vibrational frequency, depending on the phonon frequency, and usually has a magnitude of 10 THz,

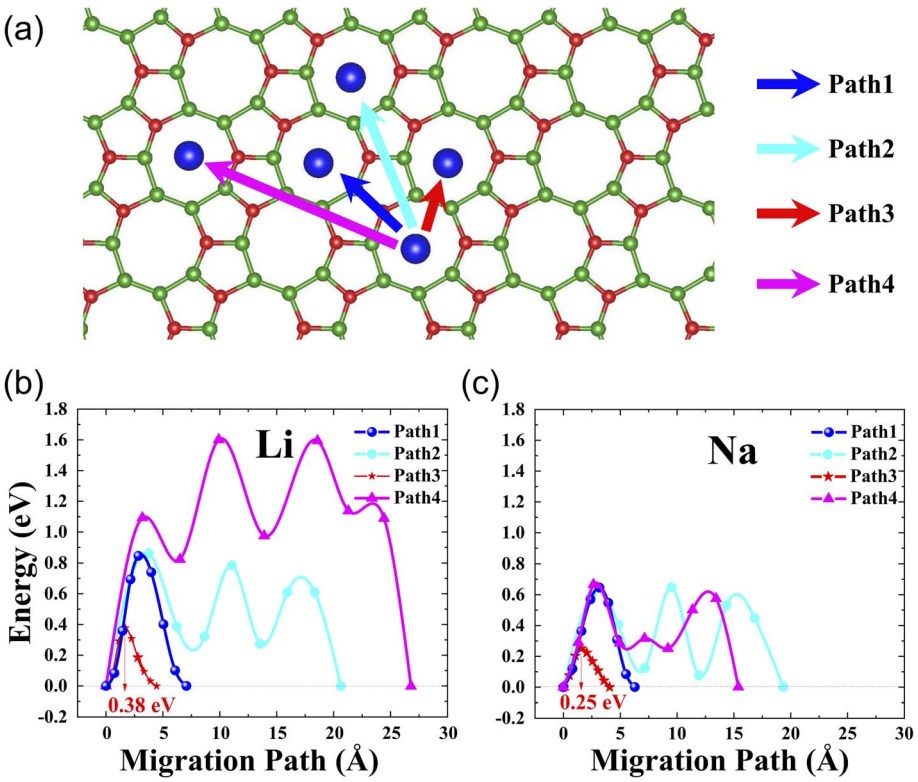

Fig. 4 (a) The considered Li/Na migration pathways correspondingly; (b) the diffusion barrier profiles for Li on l-B_2O; (c) the diffusion barrier profiles for Na on l-B_2O.

Table 2 Theoretically calculated Li/Na diffusion coefficients of l-B_2O

				Diffusion coefficient ($cm^2\ s^{-1}$)		
		d (Å)	E_a (eV)	$T = 250$ K	$T = 300$ K	$T = 350$ K
Li	Path 1	7.07	0.85	4.26×10^{-19}	2.98×10^{-16}	3.21×10^{-14}
	Path 2	20.62	0.79	6.23×10^{-17}	2.71×10^{-14}	2.08×10^{-12}
	Path 3	4.45	0.38	4.79×10^{-10}	8.90×10^{-9}	7.18×10^{-8}
	Path 4	26.79	1.60	3.81×10^{-33}	9.13×10^{-28}	6.35×10^{-24}
Na	Path 1	6.28	0.65	3.71×10^{-15}	5.51×10^{-13}	1.96×10^{-11}
	Path 2	0.65	0.39	4.86×10^{-12}	1.02×10^{-10}	8.99×10^{-10}
	Path 3	4.07	0.25	1.48×10^{-7}	1.03×10^{-6}	4.10×10^{-6}
	Path 4	15.39	0.58	6.01×10^{-13}	5.15×10^{-11}	1.24×10^{-9}

where ν_0 is chosen to be about 10^{13} Hz. For each pathway, the higher energy barrier is chosen to determine the corresponding diffusion coefficient here. The results in Table 2 indicate that the diffusion coefficients of Na are all higher than those of Li. For Li-ion batteries anode, the values of Li diffusion coefficient in graphite range from 1.12×10^{-10} to 6.05×10^{-11} $cm^2\ s^{-1}$.[49] For Na-ion batteries anode, the Na diffusion coefficients range from 10^{-6} to 10^{-11} $cm^2\ s^{-1}$ at room temperature (300 K), which are sufficiently high enough to achieve a good rate performance.

3.4 Average open-circuit voltage (OCV) and theoretical capacity

It is well known that the storage capacity and open-circuit voltage of lithium-ion or sodium-ion batteries are crucial indicators to measure their performance. To further examine these properties, based on the discussion in the last section, we now increase the concentration of the Li or Na adsorption on l-B_2O monolayer. For estimating the maximum storage capacity, we continued to use a 2×2 supercell with an increasing number of Li or Na atoms sandwiched on either side of the host. We simulate here the half-cell reaction with M/M^+ (M = Li, Na) as follows.

$$B_{16}O_8 + xM^+ + xe^- \leftrightarrow B_{16}O_8M_x \quad (3)$$

where x is the amount of intercalated atoms.

The average OCV can be obtained by computing the total energies difference before and after M intercalation. To obtain more accurate total energies value, all the configurations are fully relaxed. In addition, usually the entropy and volume effects are negligible during the reaction. Hence, the average OCV for one intercalation reaction involving xM^+ ions can be calculated from the corresponding total energies difference as follows.

$$V_{OCV} = (E_{B_{16}O_8} + xE_M - E_{B_{16}O_8M_x})/x \quad (4)$$

where again M denotes Li or Na, E_M is the average energy of Li atoms in Li or Na metals, and $E_{B_{16}O_8}$ is the total energy of l-B_2O. $E_{B_{16}O_8M_x}$ is the total energies of l-B_2O after xM adsorption.

As mentioned before, according to the adsorption energies for Li or Na adsorption and eqn (1), l-B_2O should be suitable to be utilized as an anode material for both LIBs and NIBs. As for LIBs or NIBs anode, the first considered position of adsorbed Li/Na atoms are at the top of the hollow sites (see Fig. 2) due to the least adsorption energy. In addition, the Li/Na layer could symmetrically adsorb on both the sides of the l-B_2O monolayer. After the first layer adsorption, we add more Li/Na to the host layer. For Li adsorption, we find that when we initially put more Li atoms to the host layer with higher distance than the first Li layer; all the Li atoms relaxed to the same height, as shown in Fig. 5(a). Conversely, the Na atoms are different, and a different distribution of Na atomic layers can be clearly seen. Therefore, we calculated the relationship between different numbers of embedded Li or Na and the average OCV, as shown in Fig. 5. For the case of Li-embedded, the Li-embedded voltage is basically decreasing when the number of Li-embedded is 2, 4, 8, and 12, but with 16 Li-embedded, the Li-embedded voltage becomes −0.103 V, which means that $B_{16}O_8$ can accommodate up to 12 Li-embedded. For the case of embedded Na, when the number

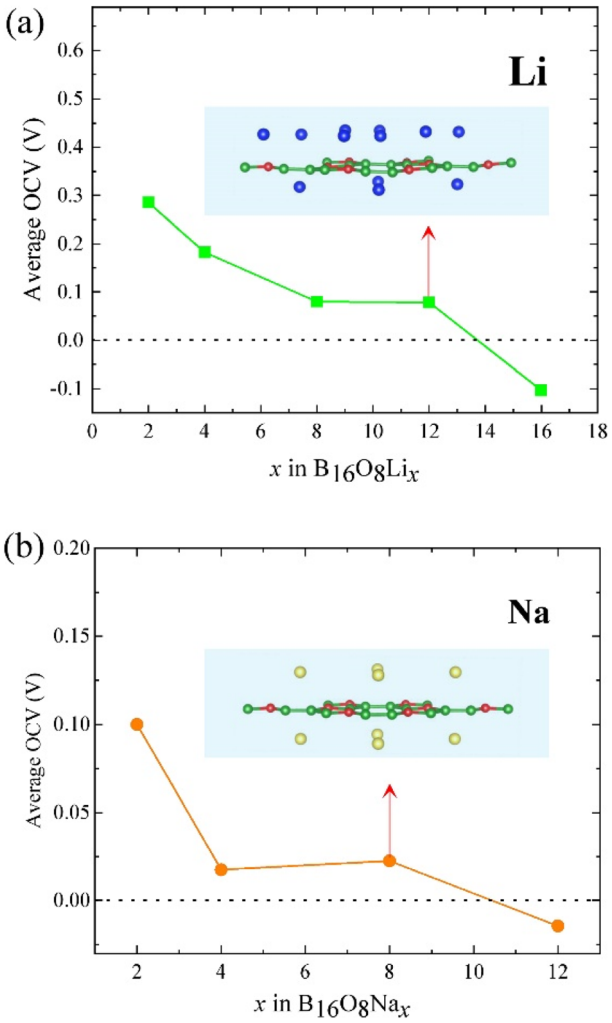

Fig. 5 The dependence of the average OCV on the number of embedded (a) Li or (b) Na, in which the embedded graph is the structure of B_2O embedded in the maximum number of embedded lithium or sodium. The blue balls here are Li atoms, the yellow ones are Na atoms, and the green and red balls are B and O atoms, respectively.

of embedded Na is 2, 4, or 8, the average OCV is also greater than 0 V; when embedded to 12, the average OCV becomes −0.003 V, indicating that the maximum number of embedded Na is 8.

Then, we can obtain the theoretical capacity (C_t) through the following equation.

$$C_t = xF/3.6M_{l\text{-}B_2O} \quad (5)$$

where x is the maximum number of electrons involving the half-cell reaction, F is the Faraday constant, and $M_{l\text{-}B_2O}$ is the mass of l-B_2O in g mol^{-1}. The calculated theoretical capacity for LIBs and NIBs are 1068.5 mA h g^{-1} and 712.33 mA h g^{-1}, respectively; the corresponding chemical formula are $B_2OLi_{1.5}$ and B_2ONa, respectively. For serving as LIBs anode, the storage capacity of l-B_2O can be 2 times that of Zr_2B_2 (526 mA h g^{-1} (ref. 50)), lower than that of β_{12}-borophene (1984 mA h g^{-1} (ref. 51)), χ_3-borophene (1240 mA h g^{-1} (ref. 51)), and Si_2BN (1158.5 mA h g^{-1} (ref. 52)). For serving as the NIBs anode, the storage capacity of l-B_2O can be higher than that of MoS_2 (146 mA h g^{-1}), Mo_2C (132 mA h g^{-1} (ref. 53)), Ti_2C (536 mA h g^{-1} (ref. 54)), and Zr_2CO_2 (474 mA h g^{-1} (ref. 55)), lower than that of phosphorene (865 mA h g^{-1}(ref. 56)) and ScC_2 (777 mA h g^{-1} (ref. 57)). In addition, we extract the information about the lattice constants from the above calculation results and then compare the changes of the lattice constants, indicating that during the intercalation and deintercalation process, the supercell lattice constants in the xy plane only change about 1.7% for Li and 0.01% for Na, respectively, which is another good advantage of l-B_2O as an anode material for both LIBs and NIBs.

4. Conclusion

In this work, we demonstrate flat 2D borophene oxide (l-B_2O) can be a very promising anode material for both LIBs and NIBs using first-principles calculations. Our study reveals that l-B_2O has good electrical conductivity before and after Li/Na adsorption, the Li/Na diffusion barrier height and average open-circuit voltage are both low, which is beneficial to the rate performance and full-cell operation voltage respectively. Furthermore, it suffers a small lattice change (<1.7%), ensuring good cycling performance. In particular, we find that the Li and Na theoretical specific capacities of l-B_2O can reach up to 1068.5 mA h g^{-1} and 712.3 mA h g^{-1}, respectively, which are almost 2–3 times higher than graphite (372 mA h g^{-1}). Thus, we suggest that l-B_2O is a promising anode material for both LIBs and NIBs.

Conflicts of interest

There are no conflicts to declare.

Acknowledgements

This work is supported by Natural Science Foundation of China (Grant No. 12264029, 12064014) and Scientific Research Fund of Jiangxi Provincial Education Department (GJJ211923).

References

1 K. M. Tan, T. S. Babu, V. K. Ramachandaramurthy, P. Kasinathan, S. G. Solanki and S. K. Raveendran, *J. Energy Storage*, 2021, **39**, 102591.
2 Z. Zhang, T. Ding, Q. Zhou, Y. Sun, M. Qu, Z. Zeng, Y. T. Ju, L. Li, K. Wang and F. Chi, *Renewable Sustainable Energy Rev.*, 2021, **148**, 111263.
3 A. A. Kebede, T. Kalogiannis, J. Van Mierlo and M. Berecibar, *Renewable Sustainable Energy Rev.*, 2022, **159**, 112213.
4 X. Qi, J. Wang, G. Królczyk, P. Gardoni and Z. Li, *J. Energy Storage*, 2022, **50**, 104682.
5 M. Q. Li, R. Shan, A. Abdulla, J. Tian and S. Gao, *J. Energy Storage*, 2023, **59**, 106560.
6 L. Lu, X. Han, J. Li, J. Hua and M. Ouyang, *J. Power Sources*, 2013, **226**, 272–288.
7 M. Li, J. Lu, Z. Chen and K. Amine, *Adv. Mater.*, 2018, **30**, 1800561.
8 G. Zhao and J. Baker, *Energy Strategy Rev.*, 2022, **40**, 100819.
9 T. Chen, Y. Jin, H. Lv, A. Yang, M. Liu, B. Chen, Y. Xie and Q. Chen, *Trans. Tianjin Univ.*, 2020, **26**, 208–217.
10 J. Li, Z. Liang and S. Xu, *Energy Rep.*, 2022, **8**, 584–596.
11 K. Du, E. H. Ang, X. Wu and Y. Liu, *Energy Environ. Mater.*, 2022, **5**, 1012–1036.
12 W. Zhang, F. Zhang, F. Ming and H. N. Alshareef, *EnergyChem*, 2019, **1**, 100012.
13 D. Pahari, P. Verma and S. Puravankara, *J. Energy Storage*, 2022, **56**, 105961.
14 S. W. Kim, D. H. Seo, X. Ma, G. Ceder and K. Kang, *Adv. Energy Mater.*, 2012, **2**, 710–721.
15 X. Li, X. Y. Wang and J. Sun, *N. Carbon Mater.*, 2021, **36**, 106–116.
16 T. Perveen, M. Siddiq, N. Shahzad, R. Ihsan, A. Ahmad and M. I. Shahzad, *Renewable Sustainable Energy Rev.*, 2020, **119**, 109549.
17 A. K. Geim, *Science*, 2009, **324**, 1530–1534.
18 P. Ares and K. S. Novoselov, *Nano Mater. Sci.*, 2022, **4**, 3–9.
19 S. Wang, S. Zhao, X. Guo and G. Wang, *Adv. Energy Mater.*, 2022, **12**, 2100864.
20 M. S. Javed, A. Mateen, S. Ali, X. Zhang, I. Hussain, M. Imran, S. S. Shah and W. Han, *Small*, 2022, **18**, 2201989.
21 E. Pomerantseva and Y. Gogotsi, *Nat. Energy*, 2017, **2**, 1–6.
22 X. Chen, H. Yu, Y. Gao, L. Wang and G. Wang, *EnergyChem*, 2022, **2**, 100071.
23 Z. Q. Wang, T. Y. Lü, H. Q. Wang, Y. P. Feng and J. C. Zheng, *Frontiers of Physics*, 2019, **14**, 1–20.
24 C. Zhong, W. Wu, J. He, G. Ding, Y. Liu, D. Li, S. A. Yang and G. Zhang, *Nanoscale*, 2019, **11**, 2468–2475.
25 J. Hu, C. Zhong, W. Wu, N. Liu, Y. Liu, S. A. Yang and C. Ouyang, *J. Phys.: Condens. Matter*, 2019, **32**, 065001.
26 L. H. Li, J. Cervenka, K. Watanabe, T. Taniguchi and Y. Chen, *ACS Nano*, 2014, **8**, 1457–1462.
27 A. Lherbier, A. R. Botello-Méndez and J. C. Charlier, *2D Mater.*, 2016, **3**, 045006.

28 W. W. Luo, G. Liu, Z. H. Xu, Z. Y. Zhou, X. Wang, C. Y. Ouyang and S. Q. Liu, *Comput. Mater. Sci.*, 2017, **140**, 261–266.
29 S. Ullah, P. A. Denis and F. Sato, *RSC Adv.*, 2019, **9**, 37526–37536.
30 S. Spitzer, A. Rastgoo-Lahrood, K. Macknapp, V. Ritter, S. Sotier, W. g. M. Hecklab and M. Lackinger, *Chem. Commun.*, 2017, **53**, 5147–5150.
31 Y. Wang, J. Lv, L. Zhu and Y. Ma, *Phys. Rev. B: Condens. Matter Mater. Phys.*, 2010, **82**, 094116.
32 Y. Wang, J. Lv, L. Zhu and Y. Ma, *Comput. Phys. Commun.*, 2012, **183**, 2063–2070.
33 Y. Wang, M. Miao, J. Lv, L. Zhu, K. Yin, H. Liu and Y. Ma, *J. Chem. Phys.*, 2012, **137**, 224108.
34 G. Kresse and D. Joubert, *Phys. Rev. B: Condens. Matter Mater. Phys.*, 1999, **59**, 1758.
35 P. E. Blöchl, *Phys. Rev. B: Condens. Matter Mater. Phys.*, 1994, **50**, 17953.
36 G. Kresse and J. Hafner, *Phys. Rev. B: Condens. Matter Mater. Phys.*, 1993, **47**, 558.
37 G. Kresse and J. Furthmüller, *Phys. Rev. B: Condens. Matter Mater. Phys.*, 1996, **54**, 11169.
38 J. P. Perdew, K. Burke and M. Ernzerhof, *Phys. Rev. Lett.*, 1996, **77**, 3865.
39 G. Kresse and D. Joubert, *Phys. Rev. B: Condens. Matter Mater. Phys.*, 1999, **59**, 1758.
40 H. J. Monkhorst and J. D. Pack, *Phys. Rev. B: Solid State*, 1976, **13**, 5188.
41 A. Togo, F. Oba and I. Tanaka, *Phys. Rev. B: Condens. Matter Mater. Phys.*, 2008, **78**, 134106.
42 F. Gao, Y. H. Wei, J. G. Du and G. Jiang, *Int. J. Hydrogen Energy*, 2021, **46**, 33486–33495.
43 Y. Luo, P. F. Liu, H. T. Li, Y. Tang, J. J. He, X. Y. Huang, B. T. Wang and L. J. Zhou, *npj Comput. Mater.*, 2020, **6**, 94.
44 P. Leidinger, M. Panighel, V. Pérez Dieste, I. J. Villar-Garcia, P. Vezzoni, F. Haag, J. V. Barth, F. Allegretti, S. Günther and L. L. Patera, *Nanoscale*, 2023, **15**, 1068–1075.
45 G. Henkelman, B. P. Uberuaga and H. Jónsson, *J. Chem. Phys.*, 2000, **113**, 9901–9904.
46 H. Wang, M. Wu, X. Lei, Z. Tian, B. Xu, K. Huang and C. Ouyang, *Nano Energy*, 2018, **49**, 67–76.
47 G. H. Vineyard, *J. Phys. Chem. Solids*, 1957, **3**, 121–127.
48 R. Kutner, *Phys. Lett. A*, 1981, **81**, 239–240.
49 P. Yu, B. N. Popov, J. A. Ritter and R. E. White, *J. Electrochem. Soc.*, 1999, **146**, 8.
50 G. Yuan, T. Bo, X. Qi, P. F. Liu, Z. Huang and B. T. Wang, *Appl. Surf. Sci.*, 2019, **480**, 448–453.
51 X. Zhang, J. Hu, Y. Cheng, H. Y. Yang, Y. Yao and S. A. Yang, *Nanoscale*, 2016, **8**, 15340–15347.
52 V. Shukla, R. B. Araujo, N. K. Jena and R. Ahuja, *Nano Energy*, 2017, **41**, 251–260.
53 Q. Sun, Y. Dai, Y. Ma, T. Jing, W. Wei and B. Huang, *J. Phys. Chem. Lett.*, 2016, **7**, 937–943.
54 Y. Xiao, Y. Ding, H. Cheng and Z. Lu, *Comput. Mater. Sci.*, 2019, **163**, 267–277.
55 Q. Meng, J. Ma, Y. Zhang, Z. Li, A. Hu, J. J. Kai and J. Fan, *J. Mater. Chem. A*, 2018, **6**, 13652–13660.
56 V. V. Kulish, O. I. Malyi, C. Persson and P. Wu, *Phys. Chem. Chem. Phys.*, 2015, **17**, 13921–13928.
57 H. Huang, H. H. Wu, C. Chi, B. Huang and T. Y. Zhang, *J. Mater. Chem. A*, 2019, **7**, 8897–8904.